Sensors and Materials, Vol. 38, No. 3 (2026) 1401–1415
MYU Tokyo

S & M 4384

Enhanced Real-time Monitoring of Laser-induced Plasma Using Combined Electric and Magnetic Fields

Chau-Shing Wang,[1] Yuan-Jen Chang,[2*] and Yi-Gang Chiu[1]

[1]Department of Electrical Engineering, National Changhua University of Education, No. 2, Shi-Da Road, Changhua City 500, Taiwan
[2]Graduate Institute of Manufacturing Technology, National Taipei University of Technology, No. 1, Sec. 3, Zhongxiao E. Rd., Taipei 10608, Taiwan

(Received September 20, 2025; accepted February 24, 2026)

Keywords: laser percussion drilling, laser-induced plasma, micromachining, magnetic field, electric field

Laser drilling is widely used in precision manufacturing industries, such as those of multilayer circuit boards, medical materials, and aerospace components. Laser drilling can easily achieve microdrilling with hole diameters smaller than 1 mm, which is unattainable with traditional mechanical drilling. Because of the high processing speed of laser drilling, real-time monitoring of the drilling process has always been a challenge. In this study, we investigate the enhancement of real-time monitoring of laser-induced plasma by integrating electric and magnetic fields. A horizontal magnetic field perpendicular to an external electric field is applied above the surface of the processed material, and a vertical probe copper electrode is used to detect the plasma. Experimental results confirm theoretical predictions, demonstrating that the combination of magnetic and electric fields enhances the plasma signal detection intensity and increases drilling depth.

1. Introduction

Drilling technology plays a crucial role in the manufacturing industry. Traditional industries rely on mechanical drilling machines; however, the contact nature of mechanical drilling causes surface damage of processed materials owing to wear and tear. In contrast, laser processing offers significant advantages, including high speed and stable energy output. As a noncontact method, laser drilling minimizes surface damage, making it widely adopted in manufacturing, automotive, and electronics industries.(1) Applications include cutting intricate shapes in diamonds(2) and drilling holes without surface cracking.(3)

The quality of laser drilling depends on various factors, such as laser pulse energy, number of pulses, pulse width, pulse frequency, type of auxiliary gas, laser focusing, and the processing material.(4) To control these factors and achieve better drilling quality, real-time monitoring of the drilling process is a crucial task and a significant challenge. Currently, several monitoring methods have been employed to monitor laser processing, such as by detecting optical emission

*Corresponding author: e-mail: yjchang@ntut.edu.tw
https://doi.org/10.18494/SAM5943

ISSN 0914-4935
https://myukk.org/

while drilling,[5,6] collecting photoacoustic signals,[7,8] and high-speed charge-coupled device (CCD) cameras.[9,10] Another method is to apply an external electric field to detect laser-induced plasma.[11–14] However, the detected plasma signal remains weak. Generally, the laser-induced plasma expansion speed is in the range of several km/s,[15] meaning that the plasma edge can move 1 μm in less than 1 ns. When the drilling hole depth reaches several hundred micrometers, the plasma's flight time extends to several hundred nanoseconds, leading to a rapid decrease in electron density. As a result, the plasma signal detected by the external electric field diminishes as the hole depth increases. Therefore, the capability of using an external electric field to monitor laser drilling is limited to a certain hole depth, making it crucial to enhance its detection depth. Therefore, in this study, we aim to enhance the plasma detection capability by introducing a magnetic field in addition to the existing external electric field. Adding a horizontal magnetic field at the location of the laser-induced plasma not only influences the motion trajectories of charged particles owing to the expected Lorentz force but also increases the plasma temperature. This temperature rise enhances the energy of electrons and ions, thereby promoting collisions between charged particles and generating more ions and electrons.[16,17]

2. Methodology

In this study, a nanosecond fiber laser (YLPN-2mj-SKAM) with a maximum energy of 2 mJ, wavelength of 1064 nm, repetition frequency set at 40 kHz, and pulse width of 250 ns was used to generate laser pulses. The specifications of the laser machine are listed in Table 1. A DC power supply is used to provide the electrode voltage to generate an electric field above the workpiece surface for detecting laser-induced plasma. The experimental setup parameters of the laser are shown in Table 2. The workpiece is SUS 304 stainless steel with the size of 30 × 30 × 2 mm^3.

A schematic diagram of the overall laser experiment setup is shown in Fig. 1. When the laser beam is focused on the workpiece, laser-induced plasma is generated above the material. At this

Table 1
Laser machine specifications.

Laser machine specifications	
Item	YLPN-2mj-SKAM
Laser source size	347 × 201 × 95 (*H*, *W*, *D*) mm^3
Maximum output power	20 W
Wavelength	1059–1062 nm
Pulse repetition frequency (PRF) range	1–1000 kHz
Pulse width range	2–500 ns

Table 2
Experimental setup parameters.

Workpiece	Laser pulse energy	Pulse repetition frequency	Pulse width	Number of pulses
304 stainless steel	1.5 mJ	40 kHz	250 ns	60
Electrode voltage	Electrode spacing	Distance between electrodes and workpiece	Magnetic strength	Electrode angle
300, 350, 400, 450 V	2 mm	0.05 mm	0.42, 0.358, 0.237 T	80°

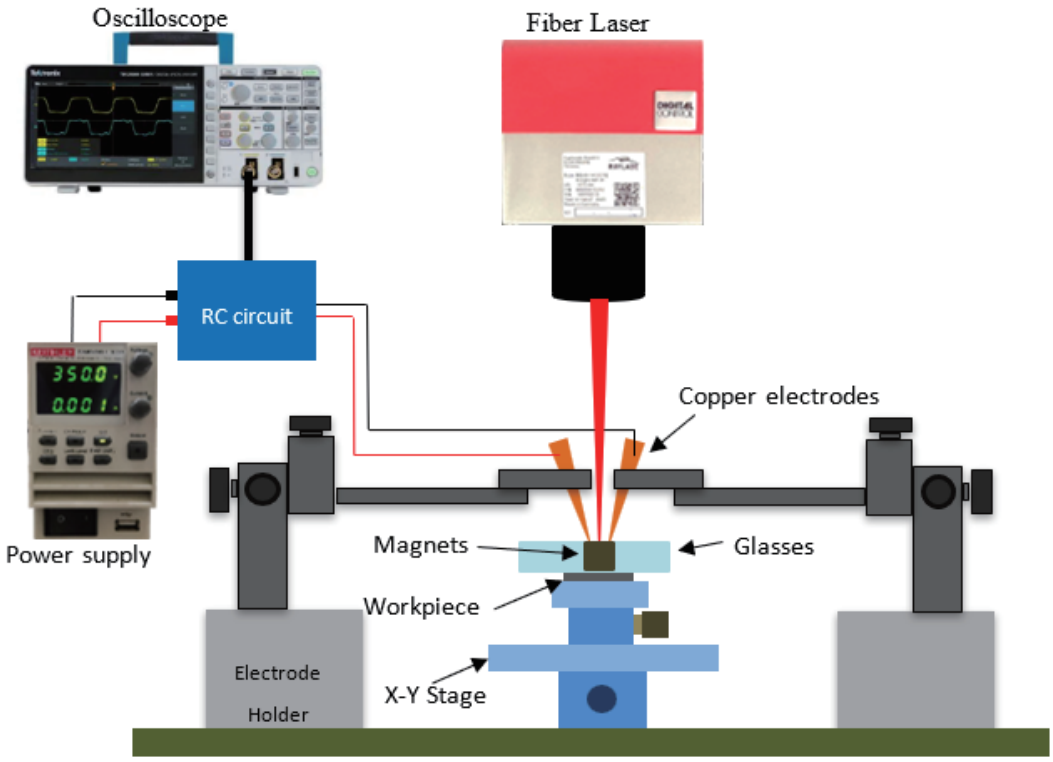

Fig. 1. (Color online) Diagram of the overall laser experiment setup.

moment, two voltage-supplied copper electrodes are used to attract the electrons and positive ions of the plasma, generating a current. This current passes through a 2 kΩ resistance of the detection circuit, forming a voltage that serves as an indicator of plasma detection, as shown in Fig. 2. The two copper electrodes are 5 cm long, 2 mm thick, and spaced 2 mm apart. In this study, to enhance the probability of electrons and positively charged ions traveling toward the positive and negative electrodes, respectively, a horizontal magnetic field perpendicular to the electric field is added above the workpiece, as shown in Figs. 3 and 4. The magnetic field is generated by several N52 neodymium magnets separated by two glass plates. We used 2, 4, and 6 magnets to obtain magnetic fields of 0.42, 0.358, and 0.237 T, respectively, measured in the surface area of the workpiece.

3. Theoretical Modeling

The plasma detection mechanism in this study utilizes an electric field generated by two copper electrodes with an applied voltage bias to attract charged particles in the plasma, thereby generating an electric current. If no voltage bias is applied to the copper electrodes, both positively and negatively charged particles may collide with the same electrode, leading to charge neutralization and preventing current generation. However, when an external voltage bias is applied to create an electric field, electrons and positively charged particles follow parabolic trajectories toward the anode and cathode electrodes, respectively, resulting in a significant

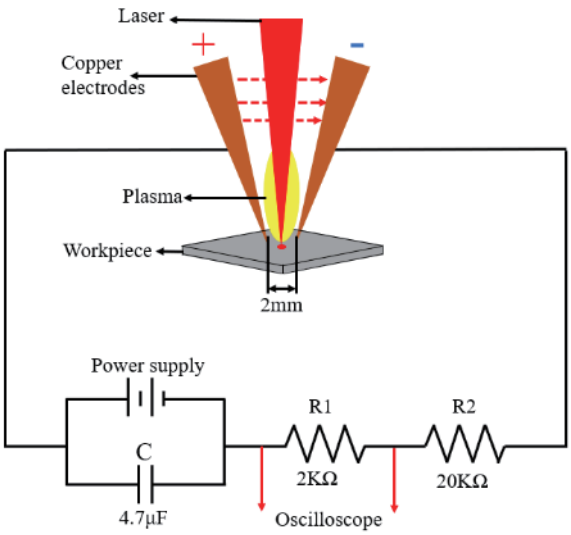

Fig. 2. (Color online) Plasma detection circuit.

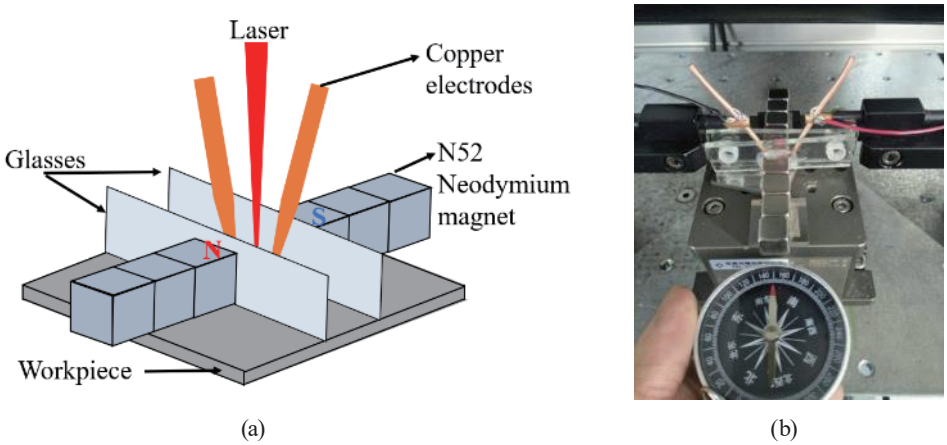

(a) (b)

Fig. 3. (Color online) Diagram of electric field and magnetic field configuration: (a) schematic diagram; three magnets placed on each side (3-3 magnets) and (b) practical setup.

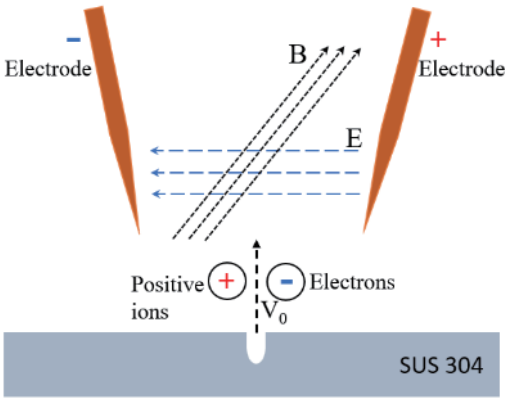

Fig. 4. (Color online) Electric field, magnetic field, and electron trajectory direction.

current. Furthermore, introducing a horizontal magnetic field perpendicular to the electric field induces a Lorentz force on the charged particles, making their trajectories even more complex.[18]

Mathematical simulations based on previous studies[19,20] were conducted to model the trajectories of charged particles of the plasma in the presence of the electric field only and the combination of electric and magnetic fields.

3.1 Effect of electric field only

In a 3D space, the electric field E is directed along the negative X-axis, and a charged particle is launched from the origin with an initial velocity v_0 in the upward direction (Z-axis). Given that the electron has mass m and charge q, the force exerted on the electron by electric field E is $F_E = qE$. Therefore, the acceleration of the electron along the X-axis is given by $a = E(q/m)$. Thus, the positions of the electron along the X-axis and Z-axis can be expressed as

$$x = 0.5 * E\left(\frac{q}{m}\right)t^2, \tag{1}$$

$$z = v_0 t \ ; \ y = 0. \tag{2}$$

It is given that the electron mass is $m = 9.11 \times 10^{-31}$ kg and its charge is $q = 1.602 \times 10^{-19}$ C. The electrodes used to detect the plasma are assumed to be a pair of flat, parallel copper plates, so that a uniform electric field can be generated. The electric field between the two electrodes with a 300, 350, 400, and 450 V potential difference and a $d = 2$ mm separation is calculated as $E = 1.69 \times 10^5$, 1.97×10^5, 2.25×10^5, and 2.53×10^5 V/m, respectively, using the electric field formula $E = V/d$. According to Ref. 21, research indicates that electrons in laser-induced plasma from stainless steel are ejected from the material surface at a velocity of approximately $v_0 = 10^6$ m/s. The positively charged ions in the laser-induced plasma from stainless steel are mostly Fe^{2+}.[21] Therefore, the value of q/m of the positively charged ions is around 2.89×10^{-7}. The simulated flight trajectories of electrons and positively charged particles in the electric field are shown in Fig. 5. There is no magnetic field in this simulation, so the magnetic field strength is set to zero. The long bars on the left and right sides of the figure represent large flat copper plate electrodes with applied voltage to generate a uniform electric field. The higher the electrode voltage, the greater the electric field generated, causing the charged particles to turn and fly towards the electrode sooner. The electrons collide with the positive electrode at a height of about 0.2–0.25 mm, but the positive particles are heavier, so they collide with the negative electrode at a height of about 5–6 mm. This simulation result will be useful in designing the electrode size and placement height in the future.

Since the plasma or charged particles ejected from the hole diffuse in a radial pattern, we also conducted simulations to observe how particles emitted at different angles are affected by the electric field and how their trajectories change. The simulation results in Fig. 6 show that electrons ejected vertically upward reach the highest collision point on the electrode, while the electrons ejected at other angles collide at lower positions on the electrode.

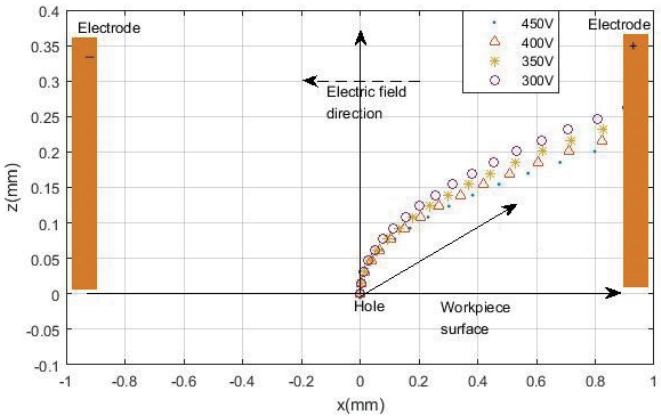

(a)

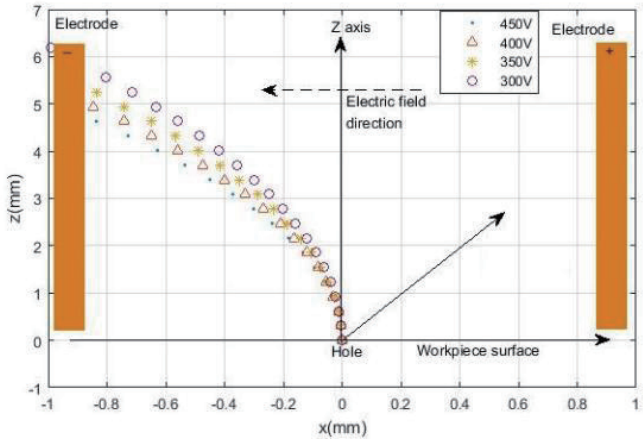

(b)

Fig. 5. (Color online) Simulated trajectories of electrons and positively charged particle in an electric field. (a) Electron trajectory and (b) positively charged particle trajectory.

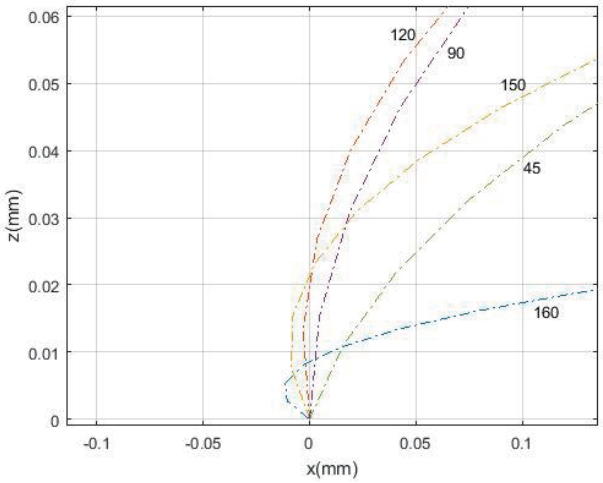

Fig. 6. (Color online) Simulated trajectories of electrons emitted at different angles within 0.1 mm of the aperture under the influence of the electric field.

3.2 Combined effect of electric and magnetic fields

When the horizontal magnetic field B perpendicular to the electric field is added to the simulation, the equations of the trajectory of the charged particles are as follows.

$$x = -\frac{m}{qB}\left(v_0 - \frac{E}{B}\right)\left[1 - \cos\left(\frac{qB}{m}t\right)\right] \tag{3}$$

$$z = \frac{E}{B}t + \frac{m}{qB}\left(v_0 - \frac{E}{B}\right)\sin\left(\frac{qB}{m}t\right); y = 0 \tag{4}$$

When the magnetic field B is directed along the negative Y-axis, the magnetic field strengths B produced by 6, 4, and 2 magnets are −0.42 T, −0.358 T, and −0.237 T, respectively. Simulation results of electrons being emitted vertically upward from the aperture with an initial velocity of $v_0 = 10^6$ m/s are shown in Fig. 7. When the magnetic field B is directed along the positive Y-axis, the magnetic field strengths B produced by 6, 4, and 2 magnets are 0.42 T, 0.358 T, and 0.237 T, respectively. These simulation results are shown in Fig. 8.

In Fig. 7, the magnetic field B is in the negative direction, so when the electron just enters the electromagnetic field, the force F_M from the magnetic field and the force F_E from the electric field are opposite, leading to the force of $F_E - F_M$. As a result, the electron moves upward in a parabolic trajectory and oscillates back and forth. This will increase the probability of the electron colliding with the electrode and enhance the detected plasma signal. In Fig. 8, the magnetic field B is in the positive direction, so when the electron just enters the electromagnetic field, the force F_M from the magnetic field and the force F_E from the electric field are in the same direction. The combination of the forces $F_E + F_M$ from the electric field and magnetic field causes the electron to immediately turn right and collide with the positive electrode along the surface of the material.

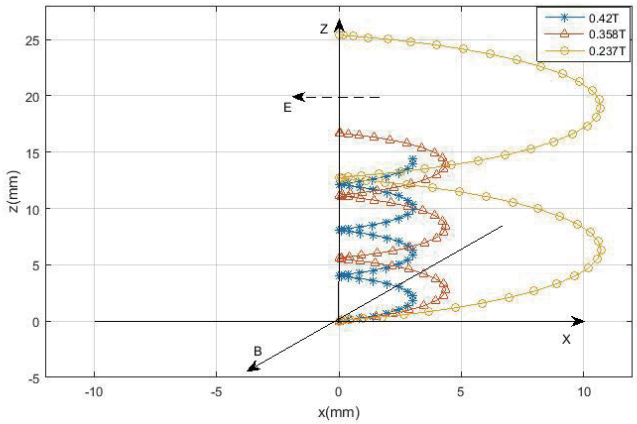

Fig. 7. (Color online) Simulated trajectories of electrons in an electromagnetic field with negative magnetic field strength.

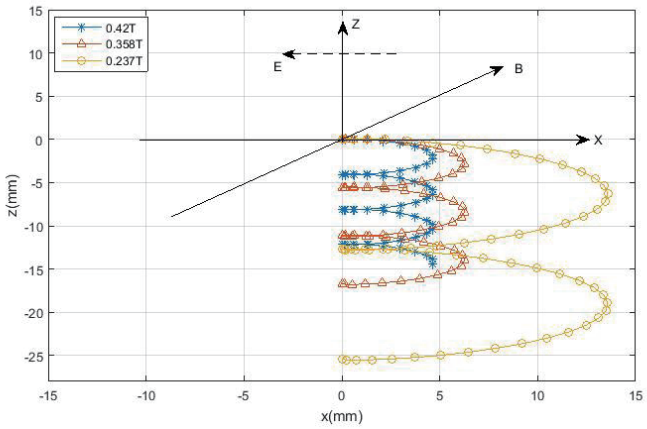

Fig. 8. (Color online) Simulated trajectories of electrons in an electromagnetic field with positive magnetic field strength.

These simulation results show that as the magnetic field increases, the amplitude of the electron's back-and-forth motion becomes more compact and more frequent, so the probability of the electron colliding with the electrode is expected to be higher.

4. Experimental Results

An oscilloscope is used to capture the detected plasma signal with the sampling rate of 6.25 MHz. Figure 9 shows the plasma signal detected using 400 V electrodes, 1.5 mJ laser energy, no magnetic field, and 60 consecutive laser pulses. Each laser pulse generates a plasma signal pulse. Figure 10 presents the curve of the peak value for each pulse.

4.1 Plasma detection with electromagnetic fields

In the experiments, the electric field was varied supplying four different voltages (300, 350, 400, and 450 V) to the copper electrodes. The detection angle of the copper electrodes was 80°. Magnetic fields of four different strengths (0.42, 0.358, 0.237, and 0 T) were generated using N52 neodymium magnets. During the experiment, the magnetic field was adjusted between the positive and reversed directions to test the differences in the detected plasma signal. The magnetic field direction along the positive *Y*-axis is defined as the positive direction (PD), while the direction along the negative *Y*-axis is defined as the reversed direction (RD). The detailed experimental parameter settings are shown in Table 2. The experiment results are shown in Figs. 11–14. In the figures, the notation "3-3" means that three magnets are placed on each side, generating a magnetic field of 0.42 T. The notation "2-2" represents 0.358 T, "1-1" represents 0.237 T, and "0-0" represents no magnetic field.

The peak values of 60 plasma pulses are summed for comparison, showing that a higher electrode voltage results in a stronger detected plasma signal. The results are shown in Fig. 15.

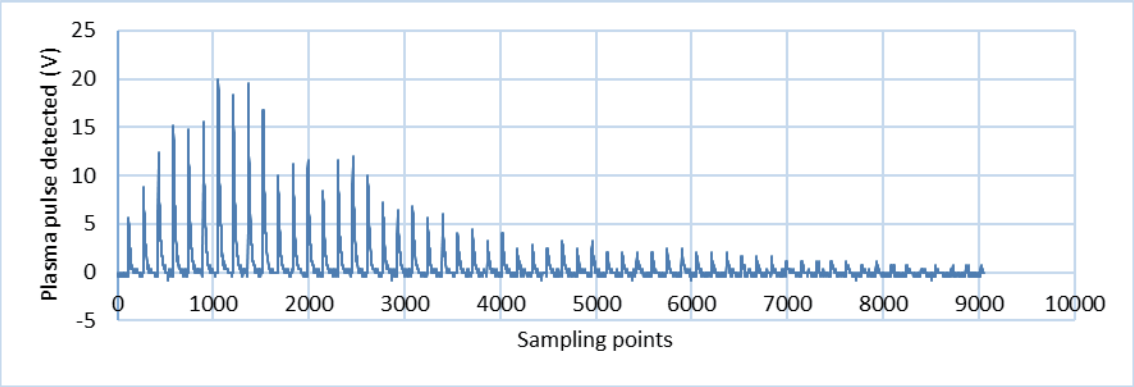

Fig. 9. (Color online) Detection signals of 60 consecutive plasma pulses.

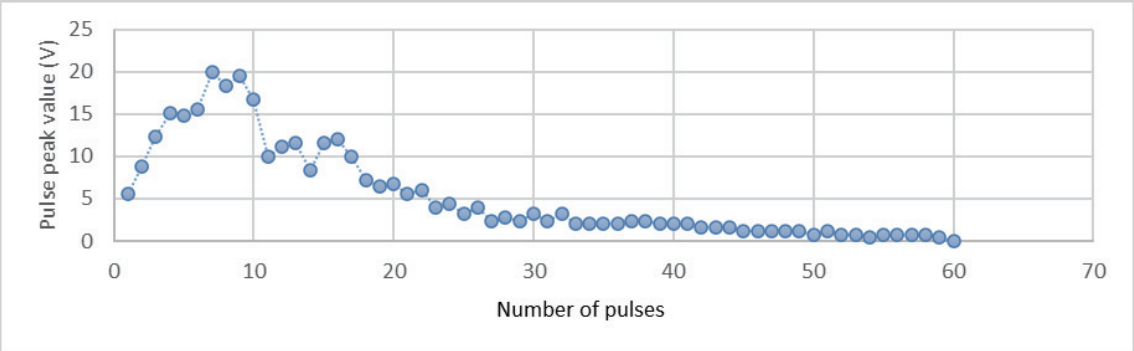

Fig. 10. (Color online) Curve of the peak value for each pulse in Fig. 9.

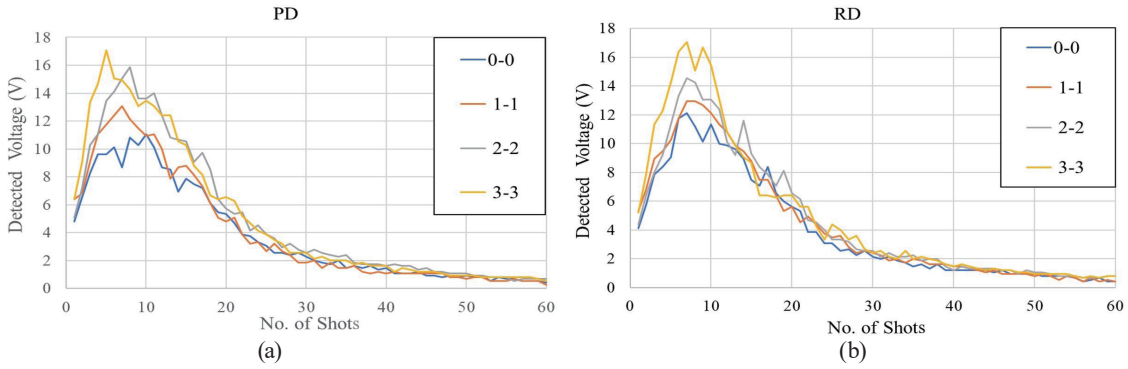

Fig. 11. (Color online) Plasma-detection signals at various magnetic field strengths (300 V electrode voltage).

The experimental results also show that the applied magnetic field significantly increases the plasma detection signal intensity, consistent with the aforementioned simulation results, indicating that the magnetic field complicates the trajectories of charged particles and increases their probability of colliding with the electrodes. For instance, under the 0.42 T magnetic field in Fig. 15, the detected plasma signal strength increased by 24, 43, 48, and 43% at the voltages of 300, 350, 400, and 450 V, respectively. Note that there is no significant difference in plasma detection signals between the PD and RD modes of the magnetic field.

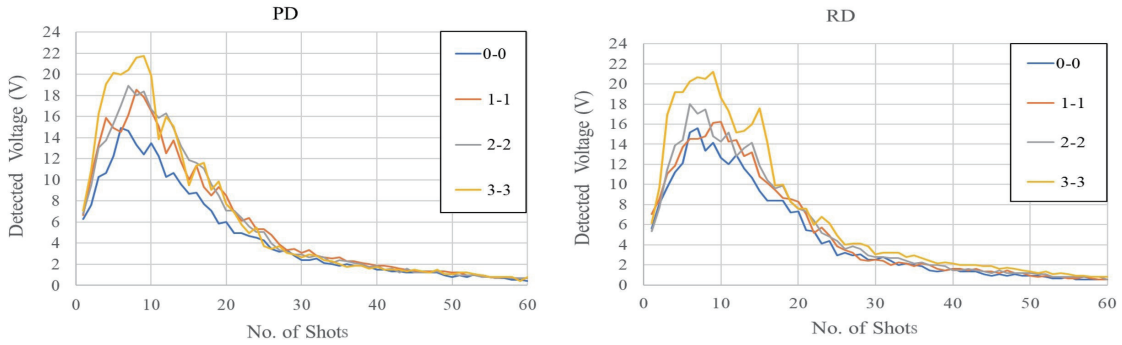

Fig. 12. (Color online) Plasma-detection signals at various magnetic field strengths (350 V electrode voltage).

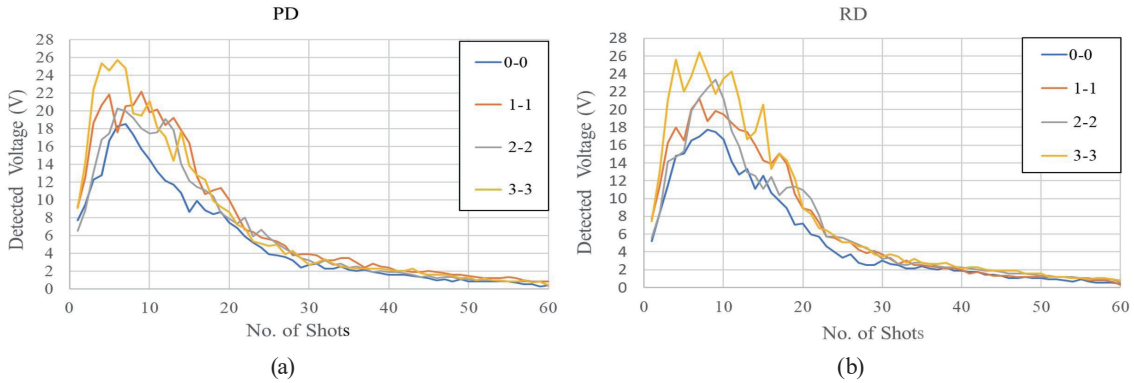

Fig. 13. (Color online) Plasma-detection signals at various magnetic field strengths (400 V electrode voltage).

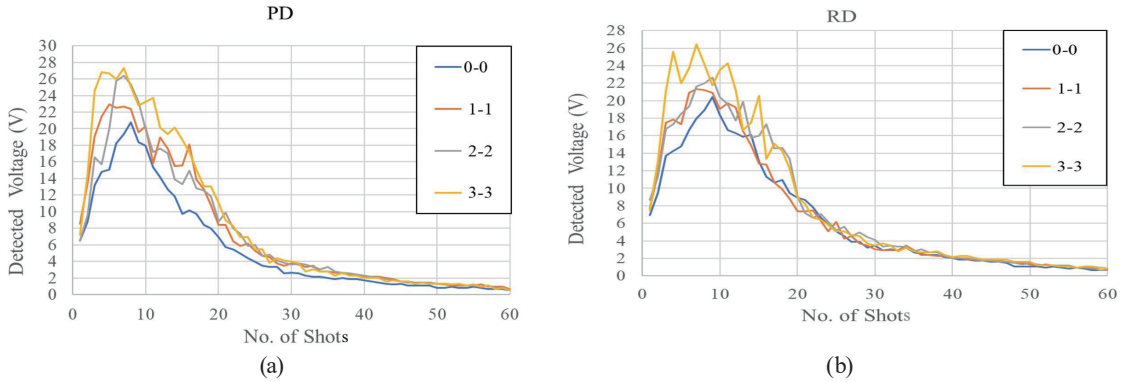

Fig. 14. (Color online) Plasma-detection signals at various magnetic field strengths (450 V electrode voltage).

4.2 Analysis of hole depth and diameter

The experimental results at a 300 V electrode voltage were analyzed to examine the effect of increasing the magnetic field on the drilling depth and hole diameter. The white light interference microscope is used to measure the hole depth and diameter. As shown in Fig. 16, the drilling hole without a magnetic field has a depth of 226.8 μm and a diameter of 56.8 μm. The

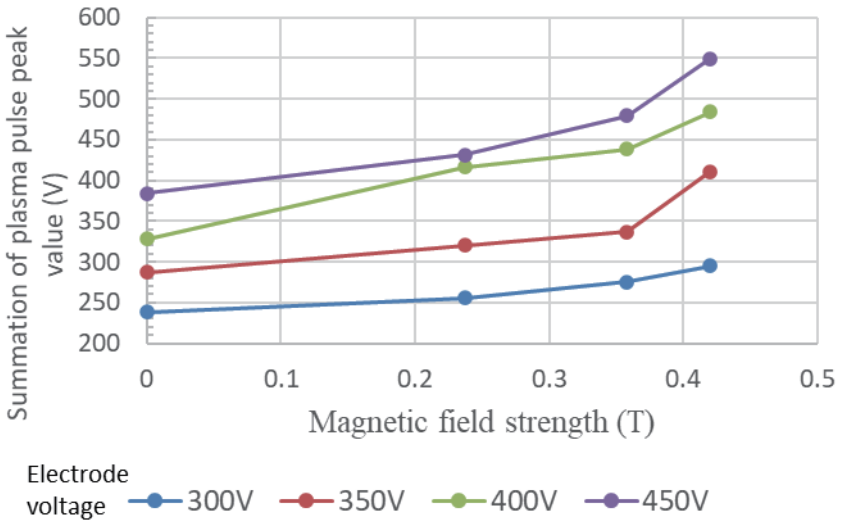

Fig. 15. (Color online) Sum of plasma pulse peak value vs magnetic field strength at various electrode voltages.

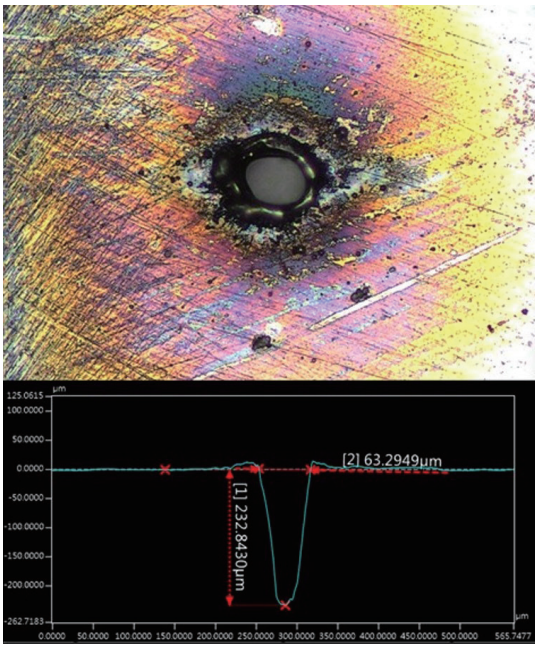

Fig. 16. (Color online) Microscope measurement results of hole depth and diameter.

measurement results of hole depth and diameter are shown in Figs. 17 and 18, respectively. Under the PD-mode magnetic field, a stronger magnetic field leads to a deeper drilling depth, while the hole diameter decreases. A possible reason is that in the PD mode, the force acting on the electrons ($F_E + F_M$) causes them to immediately turn right, while the positively charged ions turn left, leading to rapid plasma plume expansion. This reduces plasma shielding, allowing the laser beam to penetrate more effectively, thereby increasing the laser drilling depth. For example,

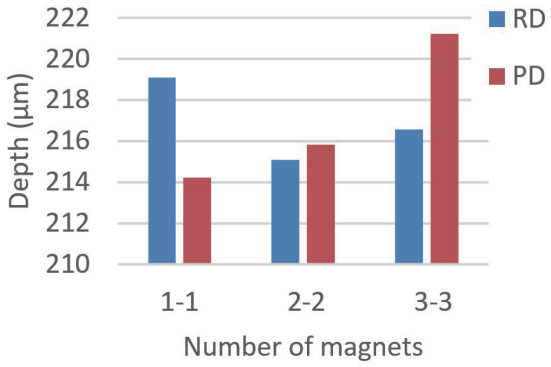

Fig. 17. (Color online) Hole depth vs number of magnets.

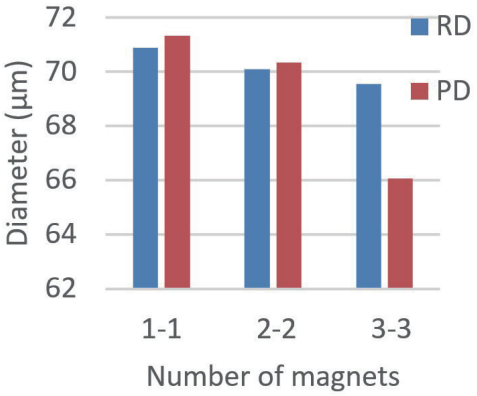

Fig. 18. (Color online) Hole diameter vs number of magnets.

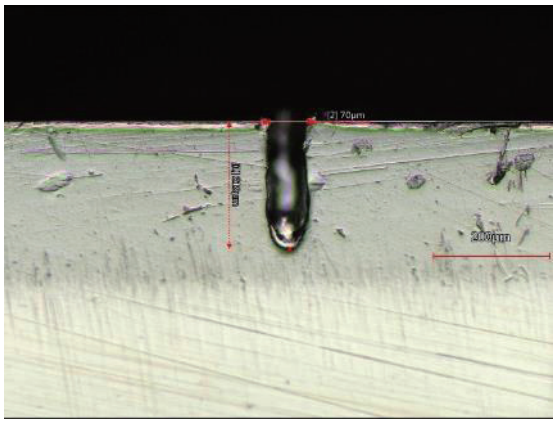

(a)

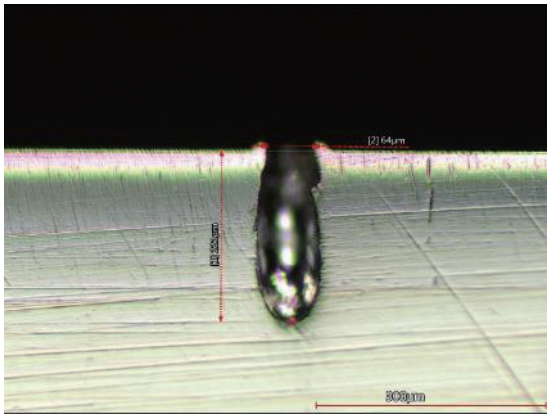

(b)

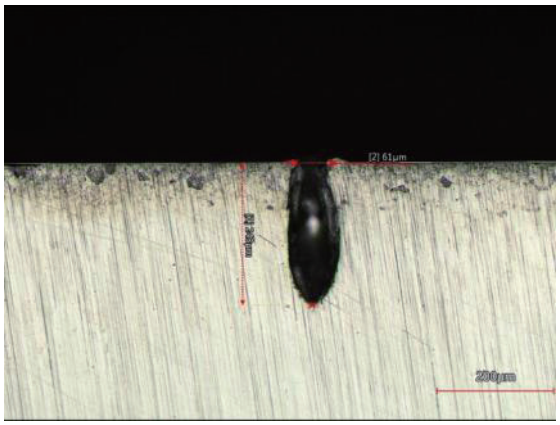

(c)

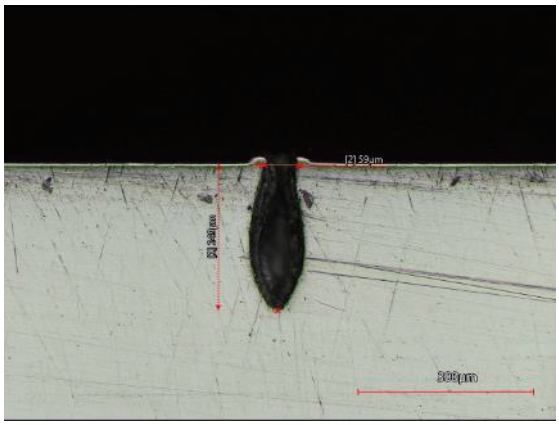

(d)

Fig. 19. (Color online) Hole cross sections in the experiment with a 350 V electrode voltage and PD-mode magnetic field with different magnetic field strengths: (a) No magnet: depth 219 μm; diameter 70 μm, (b) 1-1 magnets: depth 221 μm; diameter 64 μm, (c) 2-2 magnets: depth 243 μm; diameter 61 μm, and (d) 3-3 magnets: depth 249 μm; diameter 59 μm.

at a 300 V electrode voltage and 0.42 T magnetic field strength, the drilling depth increases to 221.23 μm compared with 210.88 μm without a magnetic field, representing a 5.2% improvement. On the other hand, a possible reason for the reduction in hole diameter is that charged molten debris disperses outward owing to the effect of the magnetic field and adheres to the hole walls earlier, causing the hole diameter to shrink. In the RD mode, the magnetic field exerts a force ($F_E - F_M$) on the electrons, resulting in a less significant effect on both hole depth and diameter.

4.2 Cross-sectional analysis of the hole

In this section, we compare the cross sections of laser-drilled holes under a 350 V electrode voltage and PD-mode magnetic field with different magnetic field strengths, as shown in Fig. 19. In the case of 0.42 T (3-3 magnets) magnetic field strength, the hole depth increased to 249 μm compared with 219 μm without a magneticc field, leading to a 13.7% improvement. The results show that as the magnetic field strength increased, the hole bottom became sharper, resulting in increased drilling depth, as described in Sect. 4.2.

5. Conclusions

We demonstrated that the integration of an external electric field with a perpendicular magnetic field significantly enhances plasma signal detection during laser drilling. First, the motion trajectories of charged particles in an electric field and an electromagnetic field were simulated, and the results indicated that the magnetic field would increase the probability of charged particles colliding with the electrodes. The actual experimental results confirmed that the capability of detecting laser-induced plasma using an electromagnetic field is better than that using only an electric field. In Fig. 15, we saw that as the magnetic field strength increased, plasma detection capability improved. For example, at a 400 V electrode voltage and a 0.42 T magnetic field, the total detected plasma voltage increased by 48%.

The experimental results also revealed that the PD-mode magnetic field can increase drilling depth. This is because the effect of the magnetic force causes charged particles to rapidly disperse, reducing plasma plume shielding, whereby the laser beam is able to penetrate the plasma more effectively and ablate the material. In contrast, the RD-mode magnetic field does not have this significant effect. By the cross-sectional analysis of the holes, it was confirmed that the PD-mode magnetic field increases the drilling depth and results in a sharper hole bottom profile, while the hole diameter at the entrance becomes smaller. Therefore, in this study, both simulation and experimental results confirmed the method's efficacy, highlighting its potential for improving real-time monitoring and control in precision laser drilling processes. Future research will be focused on utilizing the enhanced plasma signals for the adaptive control of laser parameters to further improve drilling quality.

Acknowledgments

This work was supported by the National Science and Technology Council, R.O.C. (NSTC 113-2221-E-018-007).

References

1 H. J. Wang and T. Yang: J. Eur. Ceram. Soc. **41** (2021) 4997. https://doi.org/10.1016/j.jeurceramsoc.2021.04.015
2 B. Mills, D. J. Heath, M. Feinaeugle, J. A. Grant-Jacob, and R. W. Eason: J. Laser Appl. **26** (2014) 041501. https://doi.org/10.2351/1.4893233
3 S. Chatterjee, S. S. Mahapatra, V. Bharadwaj, B. N. Upadhyay, and K. S. Bindra: Eng. Comput. **37** (2021) 1181. https://doi.org/10.1007/s00366-019-00876-6
4 P. Singh, A. Pramanik, A. K. Basak, C. Prakash, and V. Mishra: Int. J. Adv. Manuf. Technol. **106** (2020) 2133. https://doi.org/10.1007/s00170-019-04687-5
5 C. C. Ho, Y. J. Chang, J. C. Hsu, C. M. Chiu, and C. L. Kuo: Measurement **80** (2016) 251. https://doi.org/10.1016/j.measurement.2015.11.024
6 A. Stournaras, K. Salonitis, and G. Chryssolouris: Int. J. Adv. Manuf. Technol. **46** (2010) 589. https://doi.org/10.1007/s00170-009-2142-8
7 T. Steege, S. Alamri, A. F. Lasagni, and T. Kunze: Sci. Rep. **11** (2021) 14540. https://doi.org/10.1038/s41598-021-93817-3
8 Y. Cai and N. H. Cheung: Microchem. J. **97** (2011) 23. https://doi.org/10.1016/j.microc.2010.05.013
9 G. Roggero, F. Scotti, F. S. Sessa, and V. Piuri: Proc. IEEE Int. Workshop Virtual Intell. Meas. Syst. (IEEE, 2001) 41–44. https://doi.org/10.1109/VIMS.2001.924884
10 P. Poprawe: CIRP Ann. **50** (2001) 137. https://doi.org/10.1016/S0007-8506(07)62090-3
11 C. C. Ho and J. Y. Kao: Opt. Laser Technol. **163** (2023) 109344. https://doi.org/10.1016/j.optlastec.2023.109344
12 Y. J. Chang, C. S. Wang, H. Y. Chang, and Y. H. Hsiao: Lasers Eng. **57** (2024) 89. https://www.oldcitypublishing.com/journals/lie-home/lie-issue-contents/lie-volume-57-number-1-3-2024/lie-57-1-3-p-89-104/
13 C. C. Ho, G. R. Tseng, Y. J. Chang, J. C. Hsu, and C. L. Kuo: Precis. Eng. **43** (2016) 43. https://doi.org/10.1016/j.precisioneng.2015.06.008
14 C. S. Wang, Y. H. Hsiao, H. Y. Chang, and Y. J. Chang: Micromachines **13** (2022) 529. https://doi.org/10.3390/mi13040529
15 G. G. Gladush and I. Smurov: Physics of Laser Material Processing: Theory and Experiment (Springer, Berlin, 2011) Chap. 7. https://doi.org/10.1007/978-3-642-19831-1
16 S. S. Harilal, M. S. Tillack, B. O'Shay, C. V. Bindhu, and F. Najmabadi: Phys. Rev. E **69** (2004) 026413. https://doi.org/10.1103/PhysRevE.69.026413
17 M. Akhtar, A. Jabbar, N. Ahmed, S. Mehmood, Z. A. Umar, R. Ahmed, and M. A. Baig: Laser Part. Beams **37** (2019) 67. https://doi.org/10.1017/S026303461900006X
18 M. Moisan and J. Pelletier: Physics of Collisional Plasmas: Introduction to High-Frequency Discharges (Springer, Dordrecht, 2012) pp. 101–202. https://doi.org/10.1007/978-94-007-4558-2
19 G. Huang: Sci. Educ. Mon. **1** (2017) 40.
20 W. C. Fang and S. P. Huang: Friends Phys. **3** (2015) 31.
21 K. Xia, N. Ren, Q. Lin, T. Li, F. Gao, H. Yang, and S. Song: Appl. Opt. **60** (2021) 1399. https://doi.org/10.1364/AO.413661

About the Authors

Chau-Shing Wang received his B.S. degree in electrical engineering from National Cheng-Kung University, Tainan, Taiwan, in 1994, and his M.S. and Ph.D. degrees in electrical engineering from the University of Missouri–Columbia, MO, USA, in 1999 and 2003, respectively. He joined the faculty of the Department of Electrical Engineering, National Changhua University of Education, Changhua, Taiwan, in 2003, where he is now a professor. His research interests are in AI, electric power measurement, and LIP detection. (cswang@cc.ncue.edu.tw)

Yuan-Jen Chang received his B.S. degree in mechanical engineering from National Taiwan University, Taiwan, in 1996, his MS degree from the Department of Aeronautics and Astronautics of National Cheng Kung University, Taiwan, in 1998, and his Ph.D. degree in mechanical engineering from the University of Colorado at Boulder, U.S.A., in 2008. He was a member of the faculty of National Yunlin University of Science and Technology, Taiwan, from 2009 to 2023. He then joined the Graduate Institute of Manufacturing Technology of National Taipei University of Technology in 2023 as a professor. His research interests include semiconductor manufacturing technology, micro-/nanofabrication techniques, EDM, and laser processing. (yjchang@ntut.edu.tw)

Yi-Gang Chiu graduated with a bachelor's degree in electrical engineering from Ming Chi University of Technology in 2021. He then pursued a master's degree in electrical engineering at National Changhua University of Education and completed it in 2024. (asd3575287@gmail.com)